NASA Contractor Report 4284

Supersonic Flow Computations for an ASTOVL Aircraft Configuration

Sekaripuram Ramakrishnan, Sukumar R. Chakravarthy,
and Kuo-Yen Szema
Rockwell International Science Center
Thousand Oaks, California

NASA

National Aeronautics and
Space Administration

Office of Management

Scientific and Technical
Information Division

1990

SUPERSONIC FLOW COMPUTATIONS FOR
AN ASTOVL AIRCRAFT CONFIGURATION

Abstract

A unified space/time marching method has been used to solve the Euler and Reynolds-averaged Navier-Stokes equations for supersonic flow past an Advanced Short Take-Off and Vertical Landing (ASTOVL) aircraft configuration. Lift and drag values obtained from the computations compare well with wind-tunnel measurements. This report describes the entire calculation procedure starting from the geometry to final postprocessing for lift and drag. The intermediate steps include conversion from IGES to the patch specification needed for the CFD code, grid generation and solution procedure. The calculations demonstrate the capability of the method used to accurately predict design parameters such as lift and drag for very complex aircraft configurations.

Introduction

Rockwell Science Center, under contract with NASA Langley Research Center, has been developing very powerful numerical methods for the Euler equations. The research began with the development of upwind schemes of first-order accuracy based on the Osher scheme and progressed to higher order TVD (Total Variation Diminishing) schemes encompassing a variety of upwind formulations including Osher's and Roe's approximate Riemann solvers (Ref. 1). This algorithmic research culminated in the development of the EMTAC (Euler Marching Technique for Accurate Computations) code for steady inviscid supersonic flows including subsonic pocket treatment (Ref. 2). The EMTAC code was delivered to NASA Langley Research Center in 1987. Rockwell International then developed a multizone capability that was built into the EMTAC-MZ code which was initially Rockwell proprietary (Ref. 3). As part of an extension to the original contract with NASA Langley Research Center, Rockwell agreed to make EMTAC-MZ available to NASA for their use and dissemination. The EMTAC-MZ code and its usage are separately described in a user manual (Ref. 4). During this period, NASA became very interested in the study of STOVL configurations (see below) and the EMTAC-MZ was used for that purpose. Subsequently, Rockwell Science Center also developed viscous flow capability in their proprietary USA-series (Unified Solution algorithms) of flow solvers (Ref. 5). It was decided as part of the NASA Langley Research Center contract to also demonstrate the feasibility of Navier-Stokes computations for ASTOVL configrations and this forms the subject matter here.

A rationale for the interest in STOVL configurations may be found in the material quoted here from Ref. 6. "Operational flexibility of modern fighter/attack aircraft can be significantly enhanced with vertical flight capability. However, numerous studies have indicated that such improvements are minimized due to performance degradations as a result of the VTOL requirement. In an attempt to design an aircraft with military advantages of VTOL, but with minimum performance degradation, General Dynamics under contract to NASA

Ames Research Center designed Configuration E-7, a short takeoff capability and vertical landing (STOVL) aircraft. The short-takeoff capability is made possible through the use of a wingborne ejector system similar to one that was developed under an earlier contract to NASA Ames." The E-7 configuration was the only one for which detailed experimental results were known to be available and therefore was chosen for the computational study reported here. Numerical computations for one other ASTOVL configuration was carried out earlier using the Euler equations and reported in Ref. 7.

The CFD codes developed at Rockwell Science Center are based on a unified approach which simplifies the numerical simulation of complex flow fields such as those associated with STOVL configurations. We now outline this capability.

The computational method is based on a finite-volume implementation of a Total Variation Diminishing (TVD) formulation embedded in a multizone structured-grid bookkeeping framework. The Euler equations or the Reynolds-averaged form of the Navier-Stokes equations are solved using a unified unsteady and steady-state formulation which permits both time-marching and space-marching, used as appropriate. A modified Baldwin-Lomax 0-equation turbulence model was used for the viscous flow computations (Ref. 8).

The codes can operate in both time- and space-marching modes. In time-marching mode, they can be used to reach a time-asymptotic steady state or to compute the transients of a truly unsteady flow. The space-marching mode is a specialization of the Gauss-Seidel relaxation method. The basic relaxation method can be used for both time-marching and space-marching. The time-marching mode using Gauss-Seidel relaxation could include forward sweeps only, backward sweeps only, or both. This mode of operation will be referred to as the space-relaxation mode. The space-relaxation mode is further specialized to the space-marching mode by setting the time step to be very large (thereby cancelling the effect of the transient term of the Euler or the Navier-Stokes equations), by neglecting viscous terms in the marching direction (when doing a viscous flow computation), and by neglecting all hyperbolic waves which propagate against the forward marching direction. In the flux-difference split scheme employed in the USA series of codes the numerical approximation to the flux term in the marching j direction is written as $(\widehat{E}_{j+1/2} - \widehat{E}_{j-1/2})$ (the subscript $j + 1/2$ refers to the cell interface between the j cell and $(j + 1)$ cell) where

$$\widehat{E}_{j+1/2} = E_j + \Delta E^-_{j+1/2}$$

and

$$E_{j+1} - E_j = \Delta E^-_{j+1/2} + \Delta E^+_{j+1/2}$$

where the subscripts $-$ and $+$ refer to the -ve and +ve waves respectively. In the space-marching mode the effect of upstream travelling waves (-ve waves) is neglected by approximating E_{j+1} by E_j. This approach differs from the PNS (Parabolized Navier-Stokes) type of space-marching techniques, wherein the upstream propagating waves are completely eliminated by suitably modifying the governing equations.

A single pass space-marching step will give the correct solution if the physics of the flow is such that waves propagating against the marching direction are either a) nonexistent or

2

b) of negligible strength. Inviscid supersonic flow is an example of the former situation. Viscous supersonic flow, under many conditions, gives rise to the latter situation.

The space-marching mode can be used for both inviscid and viscous flows. The space-marching mode for viscous flows is different from the conventional PNS approaches in several ways even though both the current approach and the PNS approach seek to get the computational solution in one sweep through the mesh. In the space-marching methodology used in the USA-series codes, the space-marching sweep is but one of many options. The space-marching sweep is sufficient when the underlying fluid physics situation is consistent with this approach as explained earlier. Subsequent passes in space-relaxation mode can be made to assess whether one space-marching pass is enough. In fact, one can use one space-marching pass followed by many relaxation passes even for completely subsonic flows. In this case, the first pass merely serves to generate an initial solution.

A multizone approach permits great flexibility in the treatment of complex geometries. This will further be illustrated in the section on results. Complex geometric topologies can be subdivided into simpler domains which can be gridded more easily. An example is when both internal and external flows must be considered together. Even when considering only external flows, the multizone approach offers a very useful capability. When the complex topologies are broken up into simpler topologies for grid generation purposes, grids may be separately generated in each zone. A coupled multizonal grid generation procedure may also be employed in which the interzonal boundaries are not completely defined but which are obtained as part of the solution to the zonally coupled grid generation process. Only the topological relationships between the zones need be specified and not the exact location and shape of the interzonal boundaries. The space-marching and space-relaxation methods are excellent approaches for computing supersonic flows with subsonic pockets. In this mode, they are used with a grid generation procedure that generates the grid in each cross-section of the geometry, required at each step of the space-marching/relaxation process. This plane-by-plane grid generation approach can also be an effective strategy for computing subsonic and transonic flows past complex configurations such as the F-14 (Ref. 9).

Multizonal and subzonal bookkeeping also allow different solution methodologies to be used in different regions of the overall computational domain. For example, a space-marching method may be used in one zone (over a long forebody region, for example) while the time-marching approach is used for regions where predominantly subsonic flow is expected (near blunt noses and cowl lips, for example). Implicit methods may be appropriate in near-field regions (near physical surfaces such as airframes) while even explicit methods may suffice in far-field regions; the coarse grids in the far-field regions may permit reasonably large time steps to be used even when explicit schemes are employed. In fact, some zones may be excluded from solution updating methods for certain Mach number regimes because then, those regions may lie in that part of the domain which cannot be affected by the vehicle. At lower Mach numbers, for example, such zones may be in the region of influence of the vehicle. When dealing with finite-rate chemistry, in those parts of the combustor with substantial chemical reactions, the fluid-dynamics and the additional

species equations may have to be solved using a coupled implicit updating procedure. In less difficult parts of the combustor, an uncoupled implicit procedure may suffice. All this flexibility permits an expert user to utilize computational resources effectively by maximizing useful computational output while minimizing cost.

The various pointwise boundary conditions that can be specified include surface tangency (with or without slip), various surface temperature boundary conditions, wall and wake conditions for turbulence, various types of interzonal boundary conditions, subsonic and supersonic inflow and outflow boundary conditions, etc.

Preprocessing

The E-7 STOVL configuration with uncambered wing was received from General Dynamics in the IGES (Initial Graphics Exchange Specification) format (Ref. 10). The steps involved in converting the geometry data from the IGES format to the format required for the CFD codes are described below.

Step 1

The E-7 configuration geometry was defined in four separate files; one for the fuselage, one for the wing, one for the tail section, and one for the inlet. Each of these files is decoded to generate sufficient number of points (x,y,z coordinates) to accurately describe the configuration.

A typical IGES file consists of three sections, namely, global section, directory entry section and the entity section. The global section briefly describes the contents of the file and gives information about the author of the file. The directory entry section has one directory entry for each entity in the file. The directory entry for each entity is fixed in size and contains twenty fields of eight characters each spread across two consecutive eighty character lines. The purpose of this section is to provide an index for the file and to contain information on each entity. Table 1, reprou. ced from IGES manual version 4.0, page 17, gives an abbreviated listing of the fields making up the directory entry for each entity.

For the specification of the ASTOVL geometry only four entities have been used. They are Circular Arc Entity (Type 100), Line Entity (Type 110), Transformation Matrix Entity (Type 124) and Parametric Spline Curve Entity (Type 112). A circular arc (Type 100) is determined by specifying the starting point, the termination point and the arc center. In this particular instant the geometry is circular only in the transformed plane and hence one tranformation matrix (Type 124) is given for each circular arc so that the tranformed coordinates in the (x,y,z) plane can be determined. A line (Type 110) is defined by its end points. A parametric spline curve entity (Type 112) specification consists of curve type 'CTYPE' (line, quadratic, cubic, etc..), degree of continuity with respect to arc length 'H', number of dimensions 'NDIM' (2 or 3), number of segments 'N', break points of piecewise polynomial 'T(1), T(2), ..., T(N+1)', x- cordinate polynomial 'AX, BX, CX, DX' followed by y-coordinate and z-cordinate polynomials 'AY, BY, CY, DY, AZ, BZ, CZ and DZ' for

each segment. Typical output from one of the IGES files (the fuselage file) is reproduced in Table 2.

Step 2

For the fuselage entries, the coordinates are sorted by x-coordinate and duplicate entries are deleted. At this stage we have the geometry of the fuselage at several x-locations defined in the form of a number of curves which include some curves or part of curves that are inside the fuselage. Also, the curves are not specified in a continuous and unidirectional sense. A typical plot of a fuselage cross section (x=200 inches) at this stage is shown in Fig. 1.

Step 3

The wing geometry was specified in the form of wing root and tip airfoil shapes. From these, the wing cross section coordinates at various x locations were generated and added to the fuselage sorted entries. The wing planform with root and tip airfoil cross sections is shown in Fig. 2.

Step 4

The wing+fuselage (WF) coordinates are reviewed using an interactive graphics program and arranged in a clockwise sequence. Also, the geometry is reflected about y=0 and the role of y and z coordinates are interchanged to arrive at the right handed system of coordinates that is usually employed in our calculations. The upper surface of the engine was not available in the IGES file supplied by General Dynamics and hence was appropriately defined using the interactive graphics software mentioned above. The resulting collection of sequential points are split into individual patches and written into a file in a format that is compatible with the input requirements of the CFD codes. A patch is the basic unit of geometry definition for each cross-section. Each cross-section shape is broken up into several patches with any discontinuities occurring only at patch end points. For each patch, the geometry is defined in terms of a set of y and z coordinates that are inputs. See EMTAC-MZ user manual for more details. A sample of the output from this step (fuselage cross section at x=200 inches) is shown in Fig. 3. A sample of patched data in the EMTAC-MZ format is shown in Table 3.

Step 5

To gain some experience on alternative approaches to this process, the tail section was split into constant x planes using Computer Vision (CV) software running on Sun workstations. However, steps 1, 2 and 4 could also have been used for the purpose. Fig. 4 shows the tail section discretized at constant x-locations using the CV software. A typical output from CV is reproduced in Table 4. These data are sorted, split into patches and written in the format required by the solver using the interactive graphic software mentioned in Step 4.

Solution Procedure

Step 1

The entire configuration was logically divided (see Fig. 5) into four sections: A) from the nose to just ahead of the canopy, B) from end of A to the beginning of the engine, C) from beginning to end of engine, and D) end of engine to end of aircraft. The inlet section was not used in the computations since the length of the inlet section was much smaller than the grid spacing along the axial direction used in the computational procedure. Sections A, B and D were to be gridded using one zone and section C was to use a 2-zone topology.

The grid in each section was constructed automatically using an elliptic solver which generates each grid plane during the space-marching sweep. Surface grid cell distribution and pitch plane grid distribution are shown in Figures 6 & 7. The grid lines are continuous on the top half of the pitch plane. In the bottom half continuity of grid lines is maintained between sections A and B. The cross-sectional grids corresponding to Sections B and C at their interface are shown in Fig. 8. Regridding between Sections B and C and between C and D were performed automatically. The grid in Section A comprised of 60 points in the axial direction, 46 points in the circumferential direction, and 35 points in the direction normal to the body. Sections B, C and D consisted of (58 x 35 x 46), (50 x 35 x 63) and (44 x 35 x 70) grid points, respectively. For the engine a (50 x 30 x 40) grid was used. The minimum grid spacing normal to the body varied from 0.0001 in the nose region to about 0.01 in the tail region.

Step 2

The solution for Section A was computed, first using space-marching followed by not more than 50 time-relaxation iterations. The x-grid spacing was sufficient for accurate time-asymptotic computations but was not enough to resolve all gradients accurately in space-marching mode. The hybrid space/time marching approach used was therefore a very effective procedure to efficiently compute this viscous supersonic flow. At the end of the time-relaxation iterations, the solution for the last four axial planes was stored to be used for starting the computations in Section B.

Step 3

The solution for Section B was space-marched from the stored solution for the last four axial planes of Section A. This was followed by about 50 time-relaxation iterations. Sections A and B could have been combined into one section within one zone but they were individually computed in order to demonstrate one technique to fit this type of large scale computation into computers with relatively small direct access memory.

Step 4

To further demonstrate other versatile capabilities of multizone methods, Sections A and B were combined in a single multizonal computation using interzonal boundary conditions that permitted bi-directional information transfer. Twenty time-relaxation iterations were

6

performed in this mode. The last four axial planes of Section B were stored for use with Section C computations.

Step 5

The last four axial planes from Section B were used as the data base from which the solution compatible with the 2-zone grid topology of Section C was constructed. This solution was space-marched first, followed by the usual number of time-relaxation iterations. The last four planes of information were stored for use in Section D.

Step 6

The 2-zone solution of Section C was reinterpolated back to the 1-zone topology used in Section D. Section D was computed starting from this followed by one space-marching pass and about 50 time-relaxation iterations.

Remarks

Less than 50 time iterations were required in each section to obtain sufficiently converged lift and drag estimates. Global flux conservation in each zone was also monitored and found to be within a tolerance of 0.1 percent.

Postprocessing

Lift and drag are computed from the results by integrating forces at each cell face at solid surfaces. The forces acting on the insides of the engine are not accounted for in the results because a) the engine geometry was not provided in the IGES data sets and therefore had to be constructed, and b) the magnitude of the contributions from this component is not expected to be large for the conditions being simulated. Surface pressure contours were also plotted using PLOT3D and GAS graphics software.

Force Computations

Here the computational plane is denoted by (ξ, η, σ) and J is the Jacobian of the transformation.

x-direction

$$X = \int \int_S \{(p + \tau_{xx})\xi_x + \tau_{yx}\eta_x + \tau_{zx}\sigma_x\} \frac{ds}{J}$$

y-direction

$$Y = \int \int_S \{\tau_{yx}\xi_y + (p + \tau_{yy})\eta_y + \tau_{zy}\sigma_y\} \frac{ds}{J}$$

7

where p is the pressure, τ_{ab} is the shear stress in the direction b on a plane whose normal is given by the direction a, S is the body surface, the subscript on ξ, η , and σ refers to differentiation and X and Y refer to the forces in the x and y directions respectively.

Lift

$$L = Y * \cos(\alpha) - X * \sin(\alpha)$$

Drag

$$D = X * \cos(\alpha) + Y * \sin(\alpha)$$

where α is the angle of attack.

The force components from the calculated results were reconstructed in the way in which such terms are evaluated in the inviscid and viscous numerical flux terms of the flow solver.

Results

A total of four cases were considered. They are:

1) $M_\infty = 1.6$, $\alpha = 0°$, Re=2.5 million/foot

2) $M_\infty = 1.6$, $\alpha = 4.9°$, Re=2.5 million/foot

3) $M_\infty = 1.6$, $\alpha = 4.9°$, Re=0.28 million/foot

4) $M_\infty = 1.6$, $\alpha = 4.9°$, inviscid

For cases 1-3 the wall boundary conditions specified were, 1) no slip, 2) zero normal pressure gradient and 3) adiabatic wall. For the inviscid case, flow tangency was specified.

Results from the lift and drag computations for these four cases are shown in Tables 5-8.

Cases 1 and 2 are useful in analysing the effect of the angle of attack. Cases 2 and 3 bring out the effect of the Reynolds number on the predicted values of lift and drag and cases 2 and 4 enable evaluation of the usefulness of an Euler solution. The predicted and measured (Ref. 6) values of the lift and drag coefficients

$$C_l = L/(1/2\rho_\infty u_\infty^2)$$

and

$$C_d = D/(1/2\rho_\infty u_\infty^2)$$

are compared in Figs. 9 and 10. The following conclusions were arrived at from these figures and the four tables presented earlier.

1) The CFD code used does an excellent job of predicting lift and drag for the flow conditions considered here.

2) As would be expected, for the angle of attack considered here, the Reynolds number has very little effect on lift and has the effect of slightly increasing the predicted value of viscous drag.

3) At an angle of attack of zero degrees the viscous drag is about 25%, a relatively high percentage, of the total drag. The fact that the computed value of drag coefficient for this case agrees quite well with the measured values demonstrates out the accuracy of the viscous computations.

It should be mentioned here that the lift and drag coefficients were the only data available from wind tunnel tests and hence the accuracy of the numerical solutions could be evaluated using only these two quantities.

For the sake of completeness pitch plane Mach number contours are shown in Figs. 11-14. These figures clearly indicate that the code used here captures all the main features of the flow field. The nose shock, the canopy shock followed by an expansion region, shock due to the engine inlet and the shock caused by an under-expansion in the flow-through engine have all been captured well. From Figs. 11 and 12 the increase in the nose shock strength at the lower surface and the decrease in the upper surface shock strength, caused by an increase in angle of attack, can be seen. A comparison of Figs. 12, 13 and 14 shows that the overall flow is inviscid-dominated.

Concluding Remarks

A unified space/time marching method has been used to solve the Euler and Reynolds-averaged Navier-Stokes equations for supersonic flow past an Advanced Short Take-Off and Vertical Landing (ASTOVL) aircraft configuration. Lift and drag values obtained from the computations compare well with wind-tunnel measurements. The calculations demonstrate the capability of the method used to accurately predict design parameters such as lift and drag for very complex aircraft configurations. The technique of using the space-marching procedure to obtain a good initial approximation for subsequent time iterations leads to an efficient method of obtaining steady state solutions for supersonic viscous flows.

References

[1] S. R. Chakravarthy and S. Osher, "Computing With High-Resolution Upwind Schemes for Hyperbolic Equations," Proceedings of the 1983 AMS-SIAM Summer Seminar on Large-Scale Computations in Fluid Mechanics, published by American Mathematical Society in *Lectures in Applied Mathematics*, Volume 22, 1985.

[2] S. R. Chakravarthy and K.-Y. Szema, "Euler Solver for Three-Dimensional Supersonic Flows with Subsonic Pockets," *Journal of Aircraft*, Volume 24, Number 2, February 1987, pages 73-83.

[3] K.-Y. Szema, S.R. Chakravarthy, W.T. Riba, J. Byerly, and H.S. Dresser, "Multi-Zone Euler Marching Technique for Flow Over Single and Multi-body Configurations," AIAA Paper No. 87-0592, January 1987.

[4] Kuo-Yen Szema and Sukumar Chakravarthy, "A User Guide for the EMTAC-MZ CFD Code", **NASA Contractor Report 4283, 1990**.

[5] S.R Chakravarthy, K.-Y. Szema, and J.W. Haney, "Unified *Nose-to-Tail* Computational Method for Hypersonic Vehicle Applications," AIAA Paper No. 88-2564, June 1988.

[6] W.H. Foley, A.E. Albright, D.J. Powers, and C.W. Smith, "Study of Aerodynamic Technology for Single-Cruise-Engine V/STOL Fighter/Attack Aircraft," NASA CR-177367, August 1985.

[7] K.Y. Szema, S.R. Chakravarthy, D. Pan, B.L. Bihari, W.T. Riba, V.M. Akdag, and H.S. Dresser, "The Application of a Unified Marching Technique for Flow Over Complex 3-Dimensional Configurations Across the Mach Number Range," AIAA Paper 88-0276, January 1988.

[8] S.V. Ramakrishnan, U.C. Goldberg, and D.K. Ota, "Numerical Computation of Hypersonic Turbulent Flows Using Zero and One Equation Models," AIAA Paper 89-2234, August 1989.

[9] K.-Y. Szema, S.R. Chakravarthy, and B.L. Bihari, "F-14 Flow Field Simulation," AIAA Paper No. 89-0642, January 1989.

[10] B. Smith, G.R. Rinaudot, K.A. Reed, and T. Wright, "Initial Graphics Exchange Specification (IGES) Version 4.0," U.S. Department of Commerce, National Bureau of Standards, June 1988.

Table 1. Format of the directory entry section

1　　8	9　　16	17　　24	25　　32	33　　40	41　　48	49　　56	57　　64	65　　72	73　　80
(1) Entity Type Number ＃	(2) Para- meter Data ⇒	(3) Structure ＃, ⇒	(4) Line Font Pattern ＃, ⇒	(5) Level ＃, ⇒	(6) View 0, ⇒	(7) Transfor- mation Matrix 0, ⇒	(8) Label Display Assoc. 0, ⇒	(9) Status Number ＃	(10) Sequence Number D ＃
(11) Entity Type Number ＃	(12) Line Weight Number ＃	(13) Color Number ＃, ⇒	(14) Para- meter Line Count ＃	(15) Form Number ＃	(16) Reserved	(17) Reserved	(18) Entity Label	(19) Entity Subscript Number ＃	(20) Sequence Number D ＃ + 1

Nomenclature:

    (n)   - Field number n

    ＃   - Integer

    ⇒   - Pointer

    ＃, ⇒ - Integer or pointer (pointer has negative sign)

    0, ⇒ - Zero or pointer

Table 2. Typical output from IGES file

```
IGES FILE FROM ACAD.  3-D ABSOLUTE COORDINATES (X,Y,Z) ARE USED FOR      S0000001
ALL ENTITIES.  IF PROBLEMS ARE ENCOUNTERED WITH THIS FILE CONTACT THE    S0000002
PERSON WHO WROTE THE FILE (22nd FIELD IN THE G SECTION BELOW) OR CONTACTS0000003
THE PRELIMINARY DESIGN METHODS GROUP AT EX. 34560, M.Z. 2635.,           S0000004
,,10HE7FUS.SECT,10HE7FUS.IGES,10HACAD V6.4K,12HPREPROC V1.0,              G0000001
16,38,8,38,8,10HE7FUS.SECT,1.0,1,4HINCH,16,0.02,13H890623.133056,         G0000002
0.00001,540.000,,21HGENERAL DYNAMICS F.W.,4,0;                            G0000003
```

110	1	0	1	199	0	0	000000	D0000001
110	0	0	1			LINE		D0000002
110	2	0	1	224	0	0	000000	D0000003
110	0	0	1			LINE		D0000004
110	3	0	1	216	0	0	000000	D0000005
110	0	0	1			LINE		D0000006
110	4	0	1	216	0	0	000000	D0000007
110	0	0	2			LINE		D0000008
110	6	0	1	231	0	0	000000	D0000009
110	0	0	2			LINE		D0000010
110	8	0	1	231	0	0	000000	D0000011
110	0	0	1			LINE		D0000012
110	9	0	1	216	0	0	000000	D0000013
110	0	0	2			LINE		D0000014
110	11	0	1	231	0	0	000000	D0000015
110	0	0	1			LINE		D0000016
110	12	0	1	231	0	0	000000	D0000017
110	0	0	2			LINE		D0000018
110	14	0	1	230	0	0	000000	D0000019
110	0	0	1			LINE		D0000020
110	15	0	1	232	0	0	000000	D0000021
110	0	0	1			LINE		D0000022
110	16	0	1	216	0	0	000000	D0000023
110	0	0	2			LINE		D0000024
110	18	0	1	255	0	0	000000	D0000025
110	0	0	2			LINE		D0000026
110	20	0	1	233	0	0	000000	D0000027
110	0	0	1			LINE		D0000028
110	21	0	1	224	0	0	000000	D0000029
110	0	0	2			LINE		D0000030
110	23	0	1	255	0	0	000000	D0000031
110	0	0	2			LINE		D0000032
110	25	0	1	233	0	0	000000	D0000033
110	0	0	1			LINE		D0000034
110	26	0	1	224	0	0	000000	D0000035

110	0	0	2			LINE		D0000036
110	28	0	1	234	0	0	000000	D0000037
110	0	0	1			LINE		D0000038
110	29	0	1	213	0	0	000000	D0000039
110	0	0	2			LINE		D0000040
110	31	0	1	214	0	0	000000	D0000041
110	0	0	2			LINE		D0000042
110	33	0	1	224	0	0	000000	D0000043
110	0	0	2			LINE		D0000044
110	35	0	1	215	0	0	000000	D0000045
110	0	0	2			LINE		D0000046
110	37	0	1	232	0	0	000000	D0000047
110	0	0	2			LINE		D0000048
110	39	0	1	217	0	0	000000	D0000049
124	174	0	0	0	0	0	000000	D0000223
124	0	0	2			T MATRIX		D0000224
100	176	0	1	212	0	223	000000	D0000225
100	0	0	1			CIRCLE		D0000226
124	177	0	0	0	0	0	000000	D0000227
124	0	0	2			T MATRIX		D0000228
100	179	0	1	231	0	227	000000	D0000229
100	0	0	1			CIRCLE		D0000230
112	180	0	1	199	0	0	000000	D0000231
112	0	0	38			SPLINE		D0000232
112	218	0	1	199	0	0	000000	D0000233
112	0	0	37			SPLINE		D0000234
112	255	0	1	212	0	0	000000	D0000235
112	0	0	16			SPLINE		D0000236
112	271	0	1	213	0	0	000000	D0000237
112	0	0	26			SPLINE		D0000238
112	297	0	1	214	0	0	000000	D0000239
112	0	0	35			SPLINE		D0000240
112	332	0	1	255	0	0	000000	D0000241
112	0	0	70			SPLINE		D0000242
112	402	0	1	255	0	0	000000	D0000243
112	0	0	68			SPLINE		D0000244
112	470	0	1	215	0	0	000000	D0000245
112	0	0	44			SPLINE		D0000246
112	514	0	1	214	0	0	000000	D0000247
112	0	0	44			SPLINE		D0000248
112	558	0	1	213	0	0	000000	D0000249
112	0	0	44			SPLINE		D0000250
112	602	0	1	215	0	0	000000	D0000251

112	0	0	49					SPLINE	D0000252
112	651	0	1	224	0	0	000000		D0000253
112	0	0	39					SPLINE	D0000254
112	690	0	1	214	0	0	000000		D0000255
112	0	0	49					SPLINE	D0000256
112	739	0	1	222	0	0	000000		D00Cu257
112	0	0	44					SPLINE	D0000258
112	783	0	1	242	0	0	000000		D0000259
112	0	0	43					SPLINE	D0000260
112	826	0	1	241	0	0	000000		D0000261
112	0	0	50					SPLINE	D0000262
112	876	0	1	240	0	0	000000		D0000263
112	0	0	49					SPLINE	D0000264
112	925	0	1	239	0	0	000000		D0000265
112	0	0	47					SPLINE	D0000266
112	972	0	1	238	0	0	000000		D0000267
112	0	0	45					SPLINE	D0000268
112	1017	0	1	237	0	0	000000		D0000269
112	0	0	46					SPLINE	D0000270
112	1063	0	1	236	0	0	000000		D0000271
112	0	0	47					SPLINE	D0000272
112	1110	0	1	235	0	0	000000		D0000273
112	0	0	50					SPLINE	D0000274
112	1160	0	1	234	0	0	000000		D0000275
112	0	0	46					SPLINE	D0000276
112	1206	0	1	233	0	0	000000		D0000277
112	0	0	44					SPLINE	D0000278
112	1250	0	1	232	0	0	000000		D0000279
112	0	0	45					SPLINE	D0000280
112	1295	0	1	231	0	0	000000		D0000281
112	0	0	51					SPLINE	D0000282

```
110,437.500000,0.0,114.103996,437.500000,0.0,60.886002;          0000213P0000169
110,424.994995,0.0,114.474998,425.000000,0.0,58.230000;          0000215P0000170
110,337.500000,0.0,117.072998,337.500000,0.0,42.308998;          0000217P0000171
110,349.994995,0.0,116.701996,350.000000,0.0,43.611996;          0000219P0000172
110,362.505005,0.0,116.330002,362.500000,0.0,45.170998;          0000221P0000173
124,0.0,0.0,0.0,-1.000000,150.000000,-0.936939,-0.349493,0.0,     0000223P0000174
0.019716,-0.349493,0.936939,0.0,119.824181;                       0000223P0000175
100,0.0,0.0,0.0,15.445742,0.0,14.461970,5.424238;                 0000225P0000176
124,0.0,0.0,-1.000000,387.475006,0.0,-1.000000,0.0,0.002524,      0000227P0000177
-1.000000,0.0,0.0,215.174667;                                     0000227P0000178
100,0.0,0.0,0.0,166.035660,0.0,165.044922,18.111074;              0000229P0000179
```

```
112,3,1,3,16,0.0,1.000000,2.000000,3.000000,4.000000,5.000000,      0000231P0000180
6.000000,7.000000,8.000000,9.000000,10.000000,11.000000,            0000231P0000181
12.000000,13.000000,14.000000,15.000000,16.000000,-4.230000016,     0000231P0000182
0.0,0.0,0.0,0.0,-0.089878400,-0.000103787,0.000194706,              0000231P0000183
83.400001536,0.000122967,-0.004157234,-0.000009312,-4.230000016,    0000231P0000184
0.0,0.0,0.0,0.0,-0.089787480,-0.092544304,0.000241652,0.000234902,  0000231P0000185
83.395957952,-0.008498842,-0.003923867,-0.000234457,                0000231P0000186
-4.230000016,0.0,0.0,0.0,-0.181855248,-0.094075168,0.000648007,     0000231P0000187
0.000269897,83.383300768,-0.017557368,-0.004162403,-0.000191851,    0000231P0000188
-4.230000016,0.0,0.0,0.0,-0.275012512,-0.094317144,0.001112752,     0000231P0000189
0.000293985,83.361389152,-0.027133098,-0.004350931,-0.000132184,    0000231P0000190
-4.230000016,0.0,0.0,0.0,-0.367922944,-0.093129032,0.001625285,     0000231P0000191
0.000302173,83.329772960,-0.036993936,-0.004465811,-0.000059418,    0000231P0000192
-4.230000016,0.0,0.0,0.0,-0.459124512,-0.090395392,0.002161443,     0000231P0000193
0.000296652,83.288253792,-0.046841416,-0.004478399,0.000012137,     0000231P0000194
-4.230000016,0.0,0.0,0.0,-0.547061824,-0.086087144,0.002708763,     0000231P0000195
0.000270195,83.236946112,-0.056353964,-0.004396901,0.000089549,     0000231P0000196
-4.230000016,0.0,0.0,0.0,-0.630169984,-0.080291360,0.003244795,     0000231P0000197
0.000217609,83.176284784,-0.065230348,-0.004213937,0.000169382,     0000231P0000198
-4.230000016,0.0,0.0,0.0,-0.706998976,-0.073146920,0.003707402,     0000231P0000199
0.000167832,83.107009888,-0.073148048,-0.003898837,0.000218883,     0000231P0000200
-4.230000016,0.0,0.0,0.0,-0.776270656,-0.064885416,0.004125577,     0000231P0000201
0.000090595,83.030181884,-0.079866632,-0.003517233,0.000269242,     0000231P0000202
-4.230000016,0.0,0.0,0.0,-0.836939840,-0.055760708,0.004441761,     0000231P0000203
0.000011746,82.947067264,-0.085174176,-0.003051415,0.000296816,     0000231P0000204
-4.230000016,0.0,0.0,0.0,-0.888247104,-0.046101168,0.004641064,     0000231P0000205
-0.000057451,82.859138496,-0.088957136,-0.002530702,0.000301316,    0000231P0000206
-4.230000016,0.0,0.0,0.0,-0.929764608,-0.036237616,0.004747516,     0000231P0000207
-0.000131236,82.767951936,-0.091217184,-0.001994997,0.000293784,    0000231P0000208
-4.230000016,0.0,0.0,0.0,-0.961385984,-0.026461970,0.004740924,     0000231P0000209
-0.000192840,82.675033600,-0.091981872,-0.001458533,0.000270240,    0000231P0000210
-4.230000016,0.0,0.0,0.0,-0.983299840,-0.017046660,0.004631836,     0000231P0000211
-0.000238050,82.581863424,-0.091344752,-0.000946879,0.000235356,    0000231P0000212
-4.230000016,0.0,0.0,0.0,-0.995952704,-0.008220521,0.004182523,     0000231P0000213
-0.000009278,82.489807136,-0.089520112,-0.000479907,0.000194415,    0000231P0000214
-4.230000016,0.0,0.0,0.0,-1.000000000,0.000116693,0.004154690,      0000231P0000215
-0.000009278,82.400001536,-0.089896680,0.000103340,0.000194415,     0000231P0000216
0;                                                                  0000231P0000217
```

15

Table 3. Patch data in EMTAC-MZ format

```
.2000000E+03     6              X, NO. OF PATCHES
*** ZONE 1
1   16                          PATCH NO., NO. OF POINTS
 .1302650E+03     .0000000E+00
 .1302290E+03     .8070000E+00
 .1301170E+03     .1632000E+01
 .1299230E+03     .2464000E+01
 .1296420E+03     .3291000E+01
 .1292740E+03     .4099000E+01
 .1288190E+03     .4875000E+01
 .1282810E+03     .5604000E+01
 .1276660E+03     .6274001E+01
 .1269840E+03     .6874000E+01
 .1262470E+03     .7394001E+01
 .1254670E+03     .7829000E+01
 .124657CE+03     .8175003E+01
 .1238320E+03     .8431000E+01
 .1230050E+03     .8600003E+01
 .1221870E+03     .8686000E+01
2   10                          PATCH NO., NO. OF POINTS
 .1221870E+03     .8686000E+01
 .1220280E+03     .9425003E+01
 .1206180E+03     .1181000E+02
 .1188730E+03     .1412300E+02
 .1168090E+03     .1632000E+02
 .1144540E+03     .1835900E+02
 .1118490E+03     .2020200E+02
 .1090420E+03     .2181800E+02
 .1060870E+03     .2318400E+02
 .1043710E+03     .2384100E+02
```

3   30   PATCH NO., NO. OF POINTS

.1043710E+03	.2384100E+02
.1034660E+03	.2506400E+02
.1026520E+03	.2619500E+02
.1019110E+03	.2726000E+02
.1012280E+03	.2827600E+02
.1005900E+03	.2926200E+02
.9998801E+02	.3023400E+02
.9941102E+02	.3120800E+02
.9885300E+02	.3220000E+02
.9829800E+02	.3322700E+02
.9774401E+02	.3431000E+02
.9717903E+02	.3547300E+02
.9659102E+02	.3674700E+02
.9596500E+02	.3817000E+02
.9528203E+02	.3979600E+02
.9451601E+02	.4170200E+02
.9362900E+02	.4400000E+02
.9330958E+02	.4511520E+02
.9296732E+02	.4623041E+02
.9257033E+02	.4734561E+02
.9217633E+02	.4846082E+02
.9178532E+02	.4957602E+02
.9137042E+02	.5069122E+02
.9083395E+02	.5180643E+02
.9056723E+02	.5236403E+02
.9029177E+02	.5292163E+02
.8994482E+02	.5347923E+02
.8956454E+02	.5403683E+02
.8907238E+02	.5459444E+02
.8794379E+02	.5515204E+02

```
4    30                          PATCH NO., NO. OF POINTS
  .8794379E+02      .5515204E+02
  .8674860E+02      .5403683E+02
  .8633095E+02      .5292163E+02
  .8607989E+02      .5180643E+02
  .8583839E+02      .5069122E+02
  .8561373E+02      .4901842E+02
  .8547777E+02      .4790321E+02
  .8541032E+02      .4734561E+02
  .8534323E+02      .4678801E+02
  .8527647E+02      .4623041E+02
  .8521010E+02      .4567281E+02
  .8516276E+02      .4511520E+02
  .8512030E+02      .4455760E+02
  .8505904E+02      .4400000E+02
  .8510003E+02      .4286600E+02
  .8512301E+02      .4177200E+02
  .8512904E+02      .4071300E+02
  .8511600E+02      .3968400E+02
  .8508700E+02      .3867900E+02
  .8504100E+02      .3769200E+02
  .8497800E+02      .3671900E+02
  .8489703E+02      .3575300E+02
  .8480002E+02      .3479200E+02
  .8468401E+02      .3383000E+02
  .8454901E+02      .3286200E+02
  .8439500E+02      .3188300E+02
  .8422000E+02      .3088900E+02
  .8402400E+02      .2987400E+02
  .8380301E+02      .2883300E+02
  .8355701E+02      .2775900E+02
```

18

```
5    3                              PATCH NO., NO. OF POINTS
  .8355701E+02      .2775900E+02
  .6172391E+02      .2415884E+02
  .5028400E+02      .2224600E+02
6   17                             PATCH NO., NO. OF POINTS
  .5028400E+02      .2224600E+02
  .4972700E+02      .2093900E+02
  .4920100E+02      .1961300E+02
  .4871000E+02      .1827000E+02
  .4825200E+02      .1691400E+02
  .4782900E+02      .1554400E+02
  .4744200E+02      .1416200E+02
  .4709100E+02      .1276900E+02
  .4677600E+02      .1136800E+02
  .4649800E+02      .9959000E+01
  .4625600E+02      .8543003E+01
  .4605200E+02      .7123000E+01
  .4588500E+02      .5699000E+01
  .4575600E+02      .4274000E+01
  .4566300E+02      .2848000E+01
  .4560800E+02      .1423000E+01
  .4558900E+02      .0000000E+00
```

```
*** ZONE 2
1    2                                      LEFT    SIDE, NO. OF POINTS
  .7700000E+02        .2667257E+02
  .7700000E+02        .0000000E+00
2    2                                      LEFT    SIDE, NO. OF POINTS
  .7700000E+02        .0000000E+00
  .4558900E+02        .0000000E+00
3   17                                      LEFT    SIDE, NO. OF POINTS
  .4558900E+02        .0000000E+00
  .4560800E+02        .1423000E+01
  .4566300E+02        .2848000E+01
  .4575600E+02        .4274000E+01
  .4588500E+02        .5699000E+01
  .4605200E+02        .7123000E+01
  .4625600E+02        .8543001E+01
  .4649800E+02        .9959000E+01
  .4677600E+02        .1136800E+02
  .4709100E+02        .1276900E+02
  .4744200E+02        .1416200E+02
  .4782900E+02        .1554400E+02
  .4825200E+02        .1691400E+02
  .4871000E+02        .1827000E+02
  .4920100E+02        .1961300E+02
  .4972700E+02        .2093900E+02
  .5028400E+02        .2224600E+02
4    2                                      LEFT    SIDE, NO. OF POINTS
  .5028400E+02        .2224600E+02
  .7700000E+02        .2667257E+02
```

20

Table 4. Typical output from CV software

```
.4874900E+03   50
.0000000E+00        .1126200E+03
-.3530962E+01       .1122717E+03
-.6921989E+01       .1112291E+03
-.1003895E+02       .1095346E+03
-.1277090E+02       .1072702E+03
-.1504102E+02       .1045422E+03
-.1681000E+02       .1014649E+03
-.1806484E+02       .9814397E+02
-.1880692E+02       .9467176E+02
-.1905000E+02       .9112900E+02
-.2403890E+01       .1340110E+03
-.3418983E+01       .1336667E+03
-.3721630E+01       .1326105E+03
-.3860076E+01       .1315000E+03
-.3997819E+01       .1303896E+03
-.4134137E+01       .1292789E+03
-.4270080E+01       .1281682E+03
-.4404725E+01       .1270573E+03
-.4538648E+01       .1259464E+03
-.4672254E+01       .1248354E+03
-.4803964E+01       .1237241E+03
-.4934725E+01       .1226128E+03
-.5065474E+01       .1215015E+03
-.5194760E+01       .1203900E+03
-.5323469E+01       .1192784E+03
-.5404894E+01       .1181641E+03
-.5127880E+01       .1170868E+03
-.4474185E+01       .1161868E+03
-.3534595E+01       .1155914E+03
-.2442000E+01       .1153830E+03
```

```
 .0000000E+00      .1865930E+03
-.3307058E+00      .1827595E+03
-.6340456E+00      .1789305E+03
-.9086426E+00      .1751162E+03
-.1160377E+01      .1712753E+03
-.1385813E+01      .1674334E+03
-.1586453E+01      .1635904E+03
-.1761281E+01      .1597461E+03
-.1913963E+01      .1559443E+03
-.2043430E+01      .1520977E+03
-.2143381E+01      .1485818E+03
-.2228967E+01      .1449096E+03
-.2299362E+01      .1410614E+03
-.2351038E+01      .1372596E+03
-.2383315E+01      .1334104E+03
-.2399626E+01      .1295618E+03
-.2399695E+01      .1257132E+03
-.2379085E+01      .1218649E+03
-.2353126E+01      .1185087E+03
-.2308000E+01      .1146610E+03
```

Table 5. Force data for **Case 1**

| | X | | Y | |
ZONE NO.	VISCOUS	INVISCID	VISCOUS	INVISCID
1	7.18	518.81	0.01	-221.76
2	19.04	764.99	0.37	-360.73
3	186.44	1464.53	-10.03	552.45
4	213.47	-1203.89	1.74	508.04
NET	426.13	1544.44	-7.91	478.00

REFAREA =   630.6 SQ.FT   = 90806.4 SQ.IN

GAMA   = 1.4

MINF   = 1.6

CNSTNT = 4.0/(GAMA*MINF*MINF*REFAREA)   = 1.22906E-05

CD   = (426.13 + 1544.44) * CNSTNT = 0.024

CL   = (-7.91 + 478.00) * CNSTNT = 0.0058

23

Table 6. Force data for **Case 2**

ZONE NO.	X		Y	
	VISCOUS	INVISCID	VISCOUS	INVISCID
1	7.34	503.33	-0.06	-64.51
2	19.68	728.76	0.64	-137.38
3	194.48	1383.72	-1.99	7315.98
5	211.83	-1283.56	1.99	9299.95
NET	433.33	1332.25	0.58	16414.04

REFAREA =   630.6 SQ.FT   = 90806.4 SQ.IN

GAMA   = 1.4

MINF   = 1.6

CNSTNT = 4.0/(GAMA*MINF*MINF*REFAREA)   = 1.22906E-05

XFORCE = 433.33 + 1332.25 = 1765.58

YFORCE = 16414.04 +   0.58 = 16414.62

COSALF = COS(4.9)   =   0.9963

SINALF = SIN(4.9)   =   0.0854

CD   = (XFORCE*COSALF + YFORCE*SINALF) * CNSTNT = 0.0388

CL   = (YFORCE*COSALF - XFORCE*SINALF) * CNSTNT = 0.1991

Table 7. Force data for Case 3

ZONE NO.	X		Y	
	VISCOUS	INVISCID	VISCOUS	INVISCID
1	17.87	503.49	0.60	-65.13
2	36.34	726.23	1.73	-136.20
3	225.78	1358.33	4.41	7649.66
4	328.17	-1393.86	1.37	8536.99
NET	608.16	1194.19	8.11	15985.32

REFAREA = 630.6 SQ.FT = 90806.4 SQ.IN

GAMA = 1.4

MINF = 1.6

CNSTNT = 4.0/(GAMA*MINF*MINF*REFAREA) = 1.22906E-05

XFORCE = 608.16 + 1194.19 = 1802.35

YFORCE = 15985.32 + 8.11 = 15993.43

COSALF = COS(4.9) = 0.9963

SINALF = SIN(4.9) = 0.0854

CD = (XFORCE*COSALF + YFORCE*SINALF) * CNSTNT = 0.0389

CL = (YFORCE*COSALF - XFORCE*SINALF) * CNSTNT = 0.1939

25

Table 8. Force data for Case 4

ZONE NO.	X		Y	
	VISCOUS	INVISCID	VISCOUS	INVISCID
1	0.0	502.40	0.0	-65.39
2	0.0	727.09	0.0	-136.79
3	0.0	1367.28	0.0	7762.24
4	0.0	-1241.78	0.0	8324.21
NET	0.0	1354.99	0.0	15884.27

REFAREA =   630.6 SQ.FT   = 90806.4 SQ.IN

GAMA   = 1.4

MINF   = 1.6

CNSTNT = 4.0/(GAMA*MINF*MINF*REFAREA)   = 1.22906E-05

XFORCE = 1354.99

YFORCE = 15884.27

COSALF = COS(4.9)   =   0.9963

SINALF = SIN(4.9)   =   0.0854

CD   = (XFORCE*COSALF + YFORCE*SINALF) * CNSTNT = 0.0333

CL   = (YFORCE*COSALF - XFORCE*SINALF) * CNSTNT = 0.1931

26
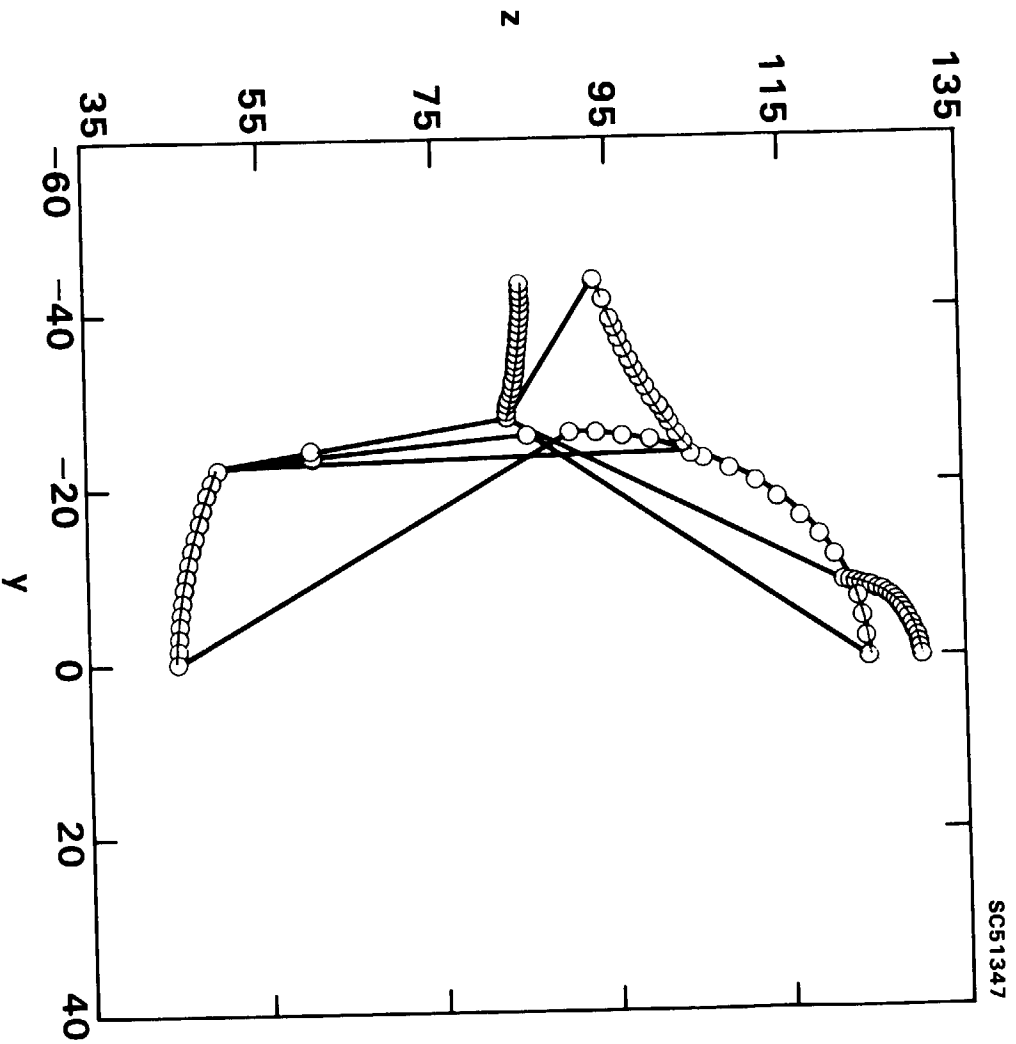
Figure 1. Fuselage cross section at $x = 200$.

SC51347

27

SC-0828-T
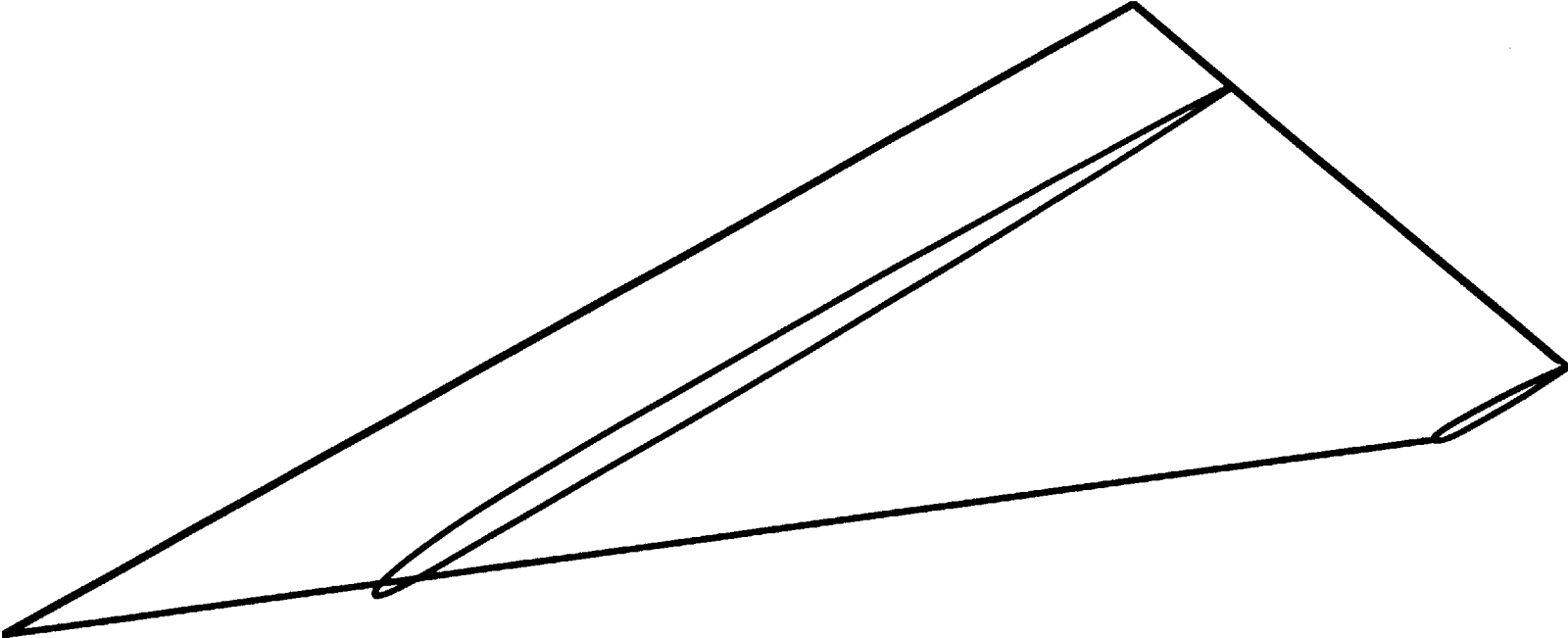
Figure 2. Wing planform.
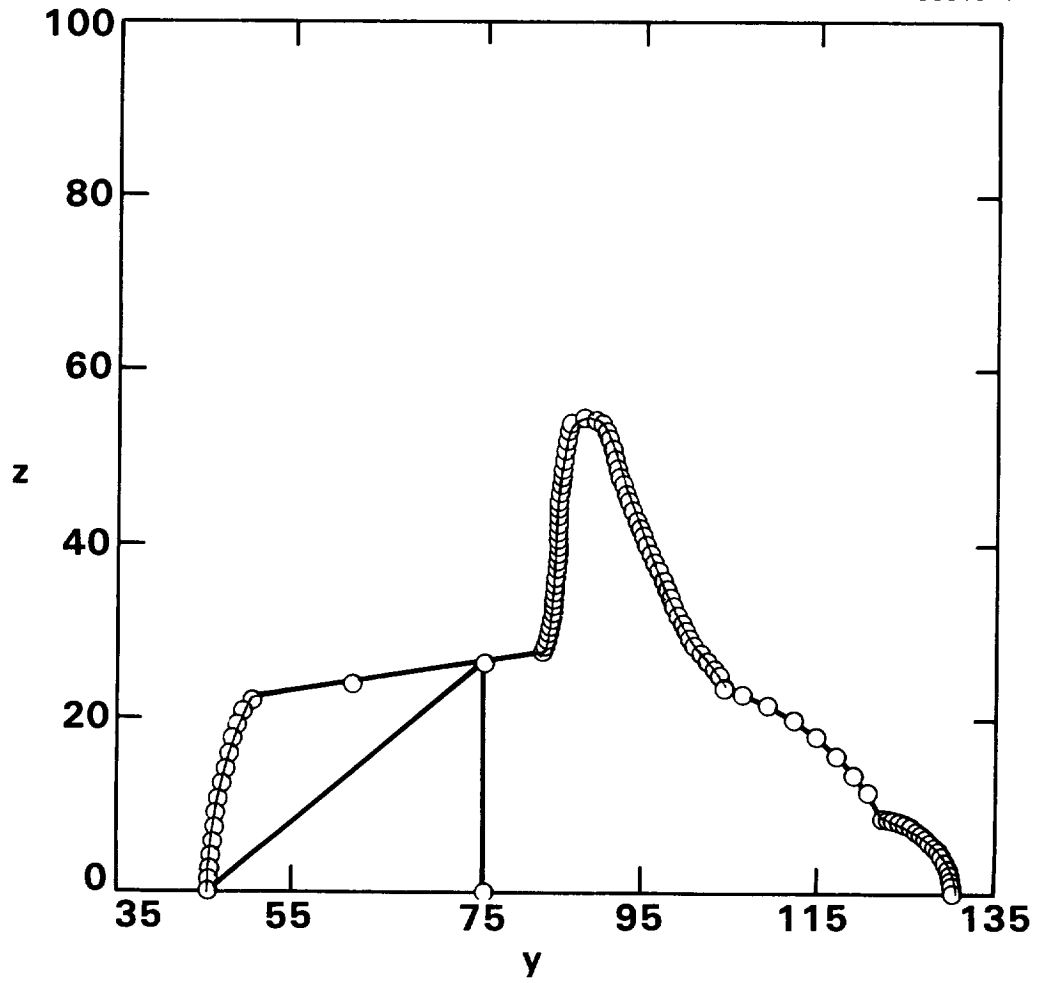
Figure 3. Fuselage cross section at $x = 200$ with wing attached.

Figure 4. Tail section.
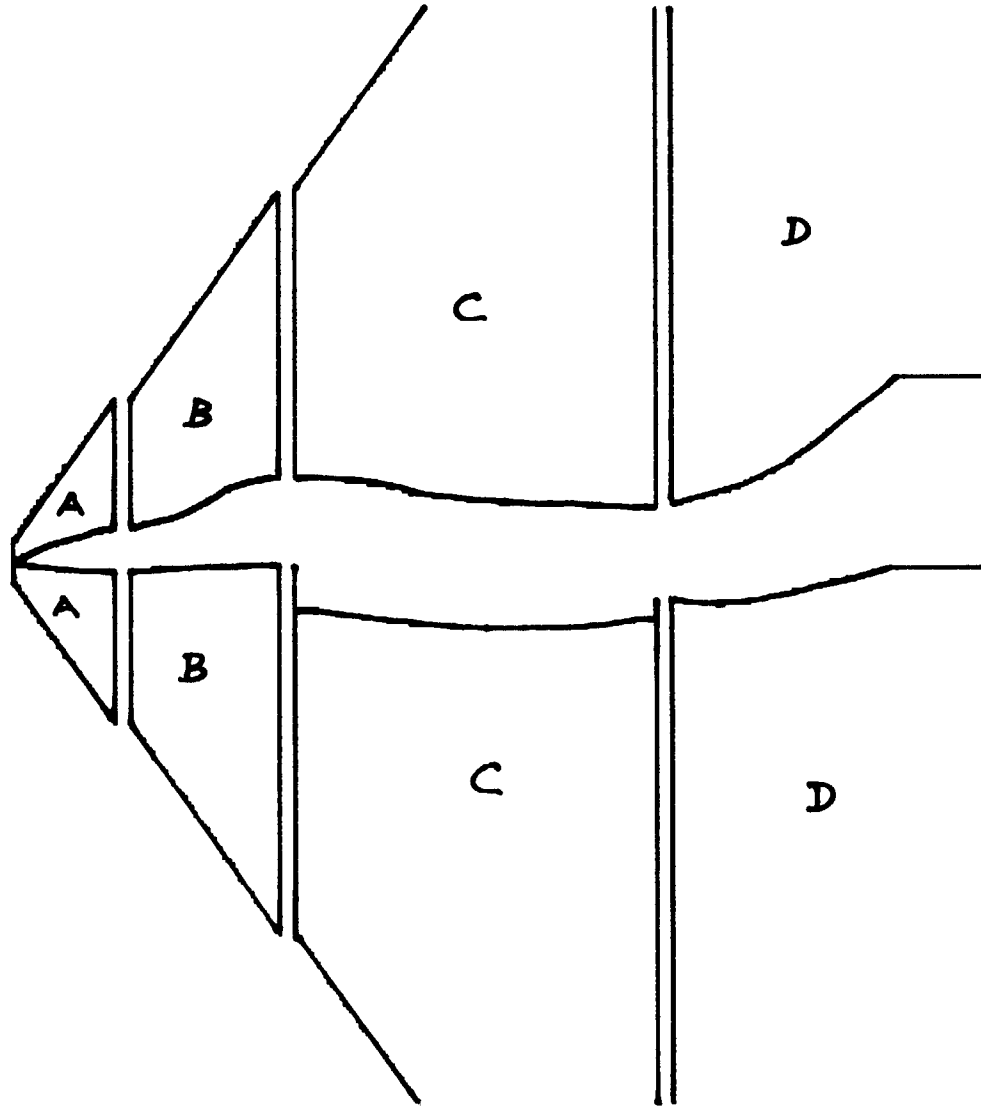
Figure 5. Zonal topology.
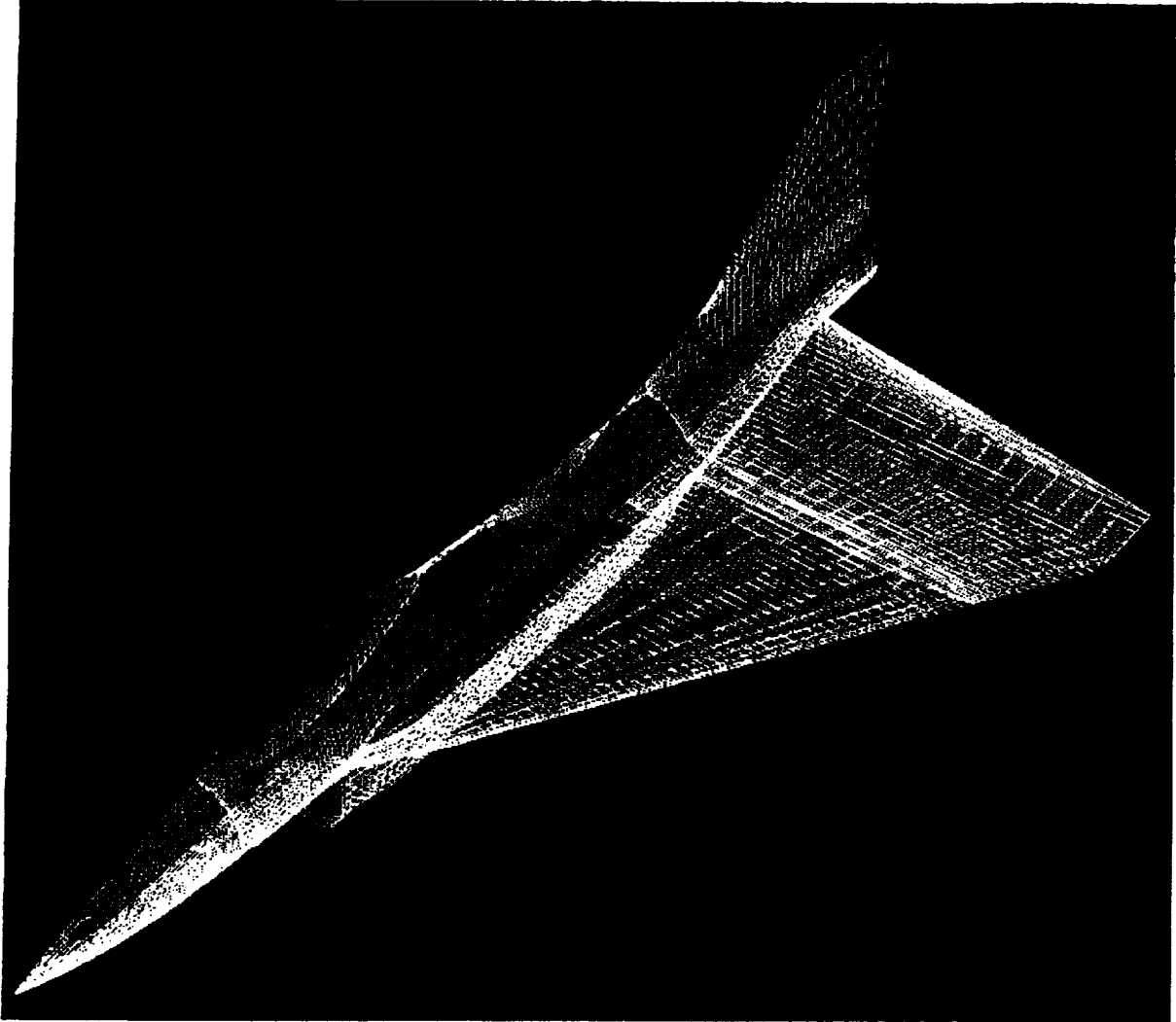
Figure 6. Surface grid.
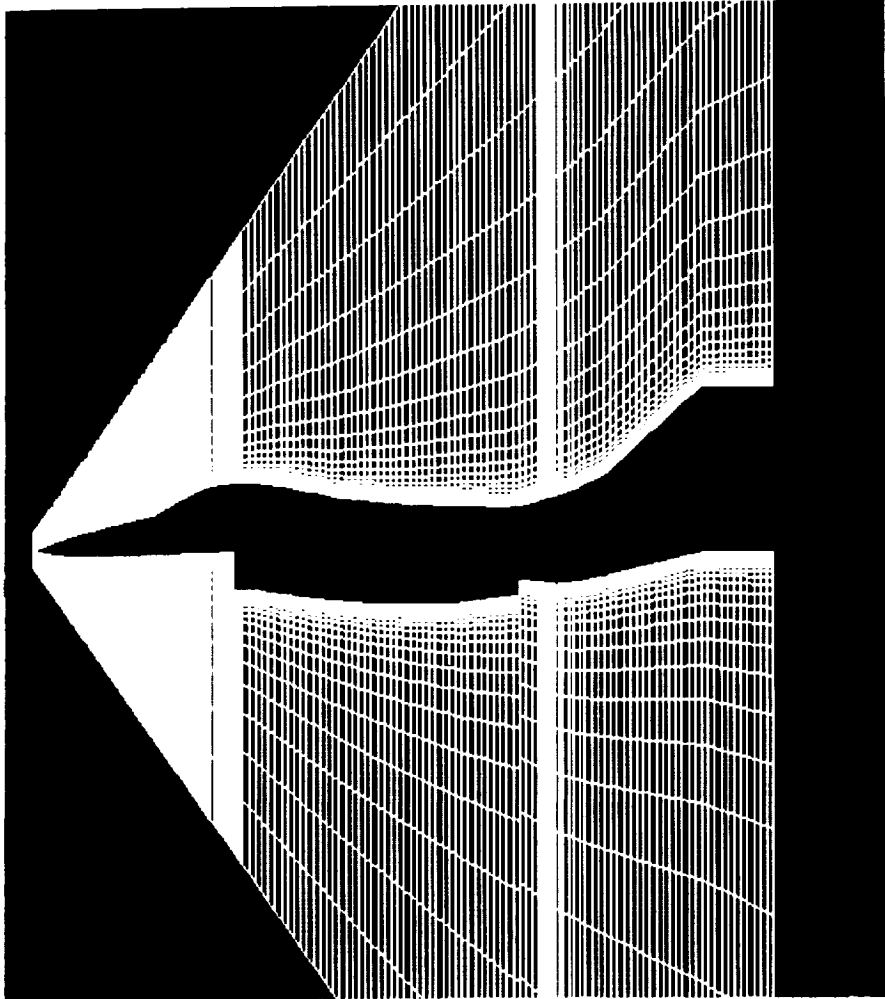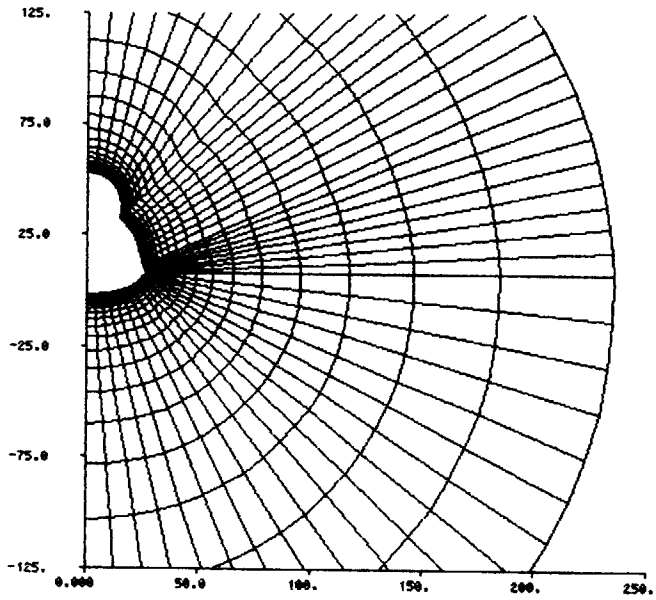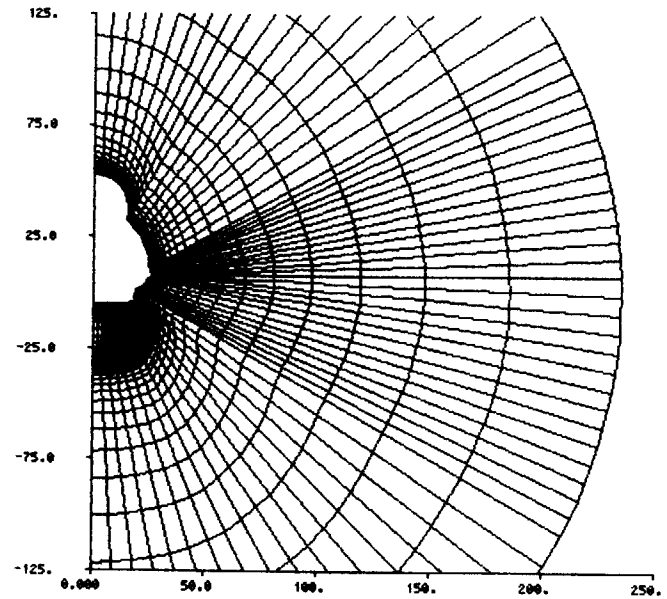
Figure 7. Pitchplane grid.

Last plane of section B   First plane of section C
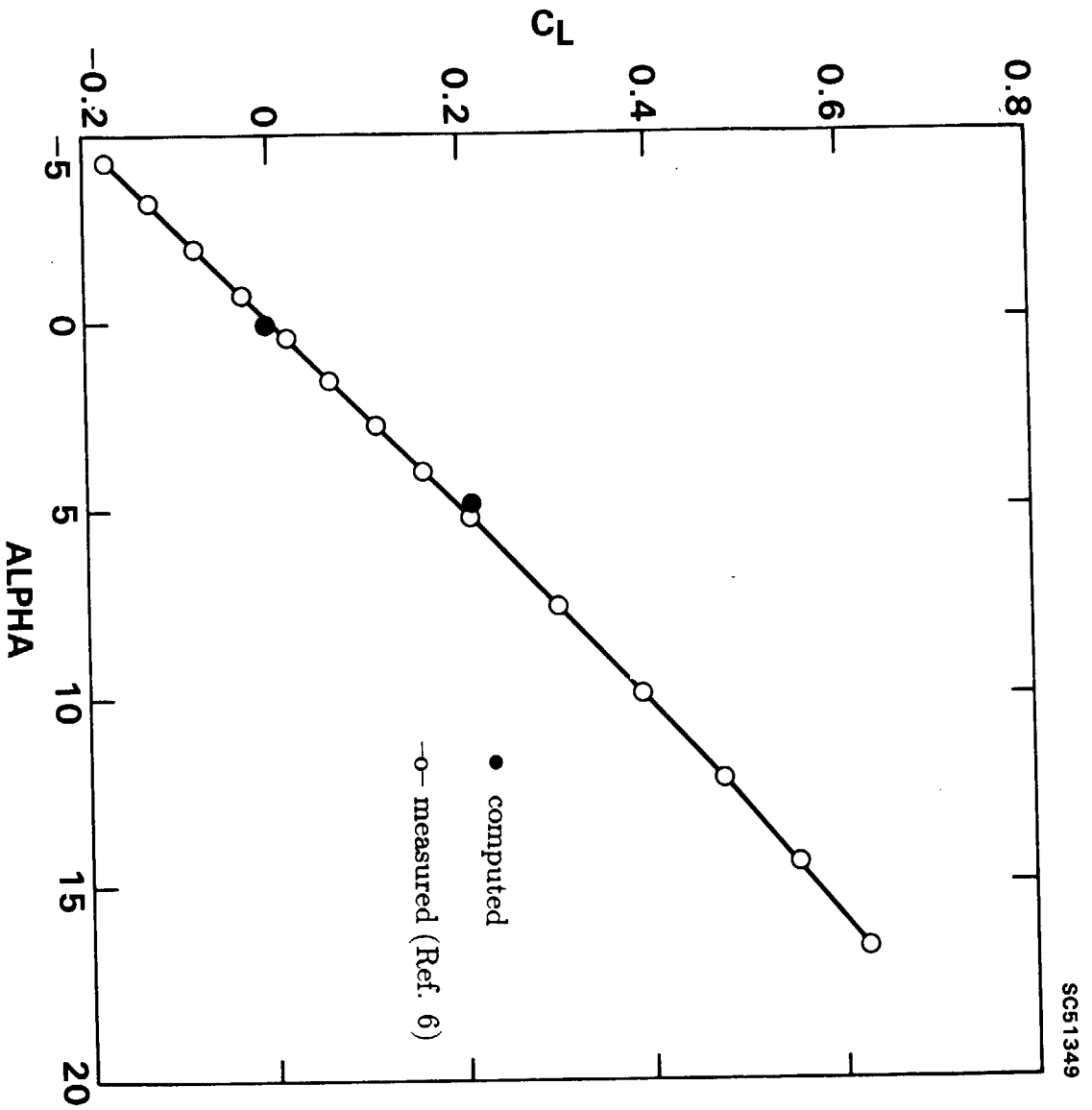
Figure 8. Cross-sectional grid.

Figure 9. C_l vs. α.

35
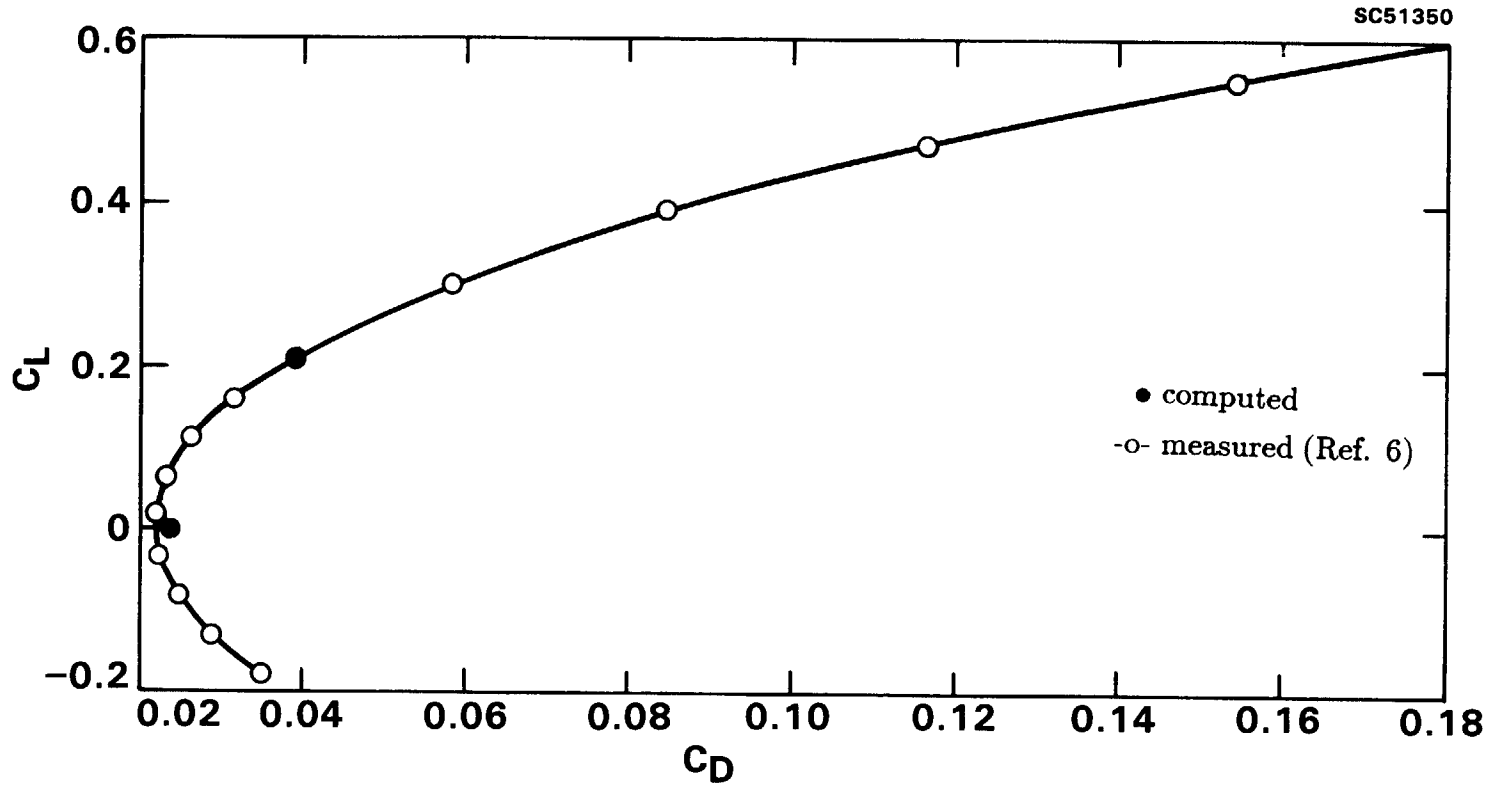
Figure 10. Drag polar.

Figure 11. Pitch plane Mach contours; $\alpha = 0°$, $Re = 2.5 million/foot$.

Figure 12. Pitch plane Mach contours; $\alpha = 4.9°$, $Re = 2.5 million/foot$.

Figure 13. Pitch plane Mach contours; $\alpha = 4.9°$, $Re = 0.28 million/foot$.

Figure 14. Pitch plane Mach contours; $\alpha = 4.9°$, inviscid.

NASA
National Aeronautics and Space Administration

Report Documentation Page

1. Report No. NASA CR-4284	2. Government Accession No.	3. Recipient's Catalog No.
4. Title and Subtitle Supersonic Flow Computations for an ASTOVL Aircraft Configuration		5. Report Date May 1990
		6. Performing Organization Code
7. Author(s) Sekaripuram Ramakrishnan, Sukumar R. Chakravarthy, and Kuo-Yen Szema		8. Performing Organization Report No.
		10. Work Unit No. 505-60-01-02
9. Performing Organization Name and Address Rockwell International Science Center 1049 Camino Dos Rios Thousand Oaks, California 91360		11. Contract or Grant No. NAS1-17492
		13. Type of Report and Period Covered Contractor Report
12. Sponsoring Agency Name and Address National Aeronautics and Space Administration Langley Research Center Hampton, Virginia 23665-5225		14. Sponsoring Agency Code

15. Supplementary Notes

Langley Technical Monitor: D.H. Rudy
Final Report (Phase II, Part 2)

16. Abstract

A unified space/time marching method has been used to solve the Euler and Reynolds-averaged Navier-Stokes equations for supersonic flow past an Advanced Short Take-Off and Vertical Landing (ASTOVL) aircraft configuration. Lift and drag values obtained from the computations compare well with wind-tunnel measurements. This report describes the entire calculation procedure starting from the geometry to final postprocessing for lift and drag. The intermediate steps include conversion from IGES to the patch specification needed for the CFD code, grid generation and solution procedure. The calculations demonstrate the capability of the method used to accurately predict design parameters such as lift and drag for very complex aircraft configurations.

17. Key Words (Suggested by Author(s)) Supersonic Flow Computations Viscous Flow Numerical Simulation	18. Distribution Statement UNCLASSIFIED — UNLIMITED Subject Category 34	
19. Security Classif. (of this report) UNCLASSIFIED	20. Security Classif. (of this page) UNCLASSIFIED	21. No. of pages 44 · 22. Price A03

NASA FORM 1626 OCT 86

NASA-Langley, 1990